ACS OMEGA

Open Access

http://pubs.acs.org/journal/acsodf

Article

Electrodeposited Copper Tin Sulfide/Reduced Graphene Oxide Nanospikes for a High-Performance Supercapacitor Electrode

Endale Kebede Feyie,* Lemma Teshome Tufa, Jaebeom Lee, Aschalew Tadesse, and Enyew Amare Zereffa*

Cite This: *ACS Omega* 2024, 9, 9452−9462

Read Online

ACCESS | Metrics & More | Article Recommendations | Supporting Information

ABSTRACT: Copper tin sulfide, Cu_4SnS_4 (CTS), a ternary transition-metal chalcogenide with unique properties, including superior electrical conductivity, distinct crystal structure, and high theoretical capacity, is a potential candidate for supercapacitor (SC) electrode materials. However, there are few studies reporting the application of Cu_4SnS_4 or its composites as electrode materials for SCs. The reported performance of the Cu_4SnS_4 electrode is insufficient regarding cycle stability, rate capability, and specific capacity; probably resulting from poor electrical conductivity, restacking, and agglomeration of the active material during continued charge−discharge cycles. Such limitations can be overcome by incorporating graphene as a support material and employing a binder-free, facile, electrodeposition technique. This work reports the fabrication of a copper tin sulfide-reduced graphene oxide/nickel foam composite electrode (CTS−rGO/NF) through stepwise, facile electrodeposition of rGO and CTS on a NF substrate. Electrochemical evaluations confirmed the enhanced supercapacitive performance of the CTS−rGO/NF electrode compared to that of CTS/NF. A remarkably improved specific capacitance of 820.83 F g^{-1} was achieved for the CTS−rGO/NF composite electrode at a current density of 5 mA cm^{-2}, which is higher than that of CTS/NF (516.67 F g^{-1}). The CTS−rGO/NF composite electrode also exhibited a high-rate capability of 73.1% for galvanostatic charge−discharge (GCD) current densities, ranging from 5 to 12 mA cm^{-2}, and improved cycling stability with over a 92% capacitance retention after 1000 continuous GCD cycles; demonstrating its excellent performance as an electrode material for energy storage applications, encompassing SCs. The enhanced performance of the CTS−rGO/NF electrode could be attributed to the synergetic effect of the enhanced conductivity and surface area introduced by the inclusion of rGO in the composite.

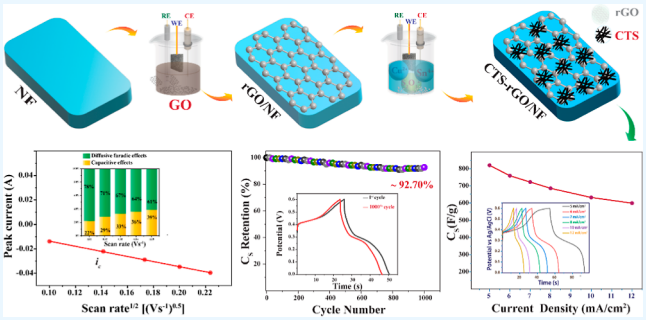

1. INTRODUCTION

The ever-rising global population and introduction of new technologies along with concerns of environmental pollution have intensified the demand for environmentally friendly alternative electricity generation, storage, and conversion materials. This has led to intense research on energy storage and conversion technologies, including batteries and supercapacitors (SCs). Although batteries are the most utilized and preferred devices for energy conversion and storage, owing to delivery of high energy density and long-term charge storage, they are limited by their lower power density, short life cycle, and therefore not suitable for applications requiring high-power delivery.[1] SCs on the contrary present a number of great advantages including long life cycle, high power density, high efficiency, high specific capacitance, low maintenance cost, flexible operating temperature, quick charging, and fast power delivery.[1−3] Hence, SCs are ideal for applications that require short-term power boosts, such as emergency power supplies and peak power assistance for batteries in electric vehicles.[1−3] Despite their benefits, SCs suffer from the drawbacks of lower energy density and higher cost;[3−6] therefore, it is highly desirable to improve the energy density of SCs to approach that of batteries, which could enable their use as a primary power source.

The performance of a SC device depends on the electrode, electrolyte used, and the working potential range, among which the type and characteristics of the electrode material and the method of preparation play a significant role.[2] Electrode materials that have been used for pseudocapacitor applications include transition-metal oxides/hydroxides,[7−10] transition-metal sulfides,[11−15] and conducting polymers.[2,5,16] Transition-metal oxides/hydroxides have proved as excellent materials for pseudocapacitor application with average

Received: November 12, 2023
Revised: January 17, 2024
Accepted: January 23, 2024
Published: February 12, 2024

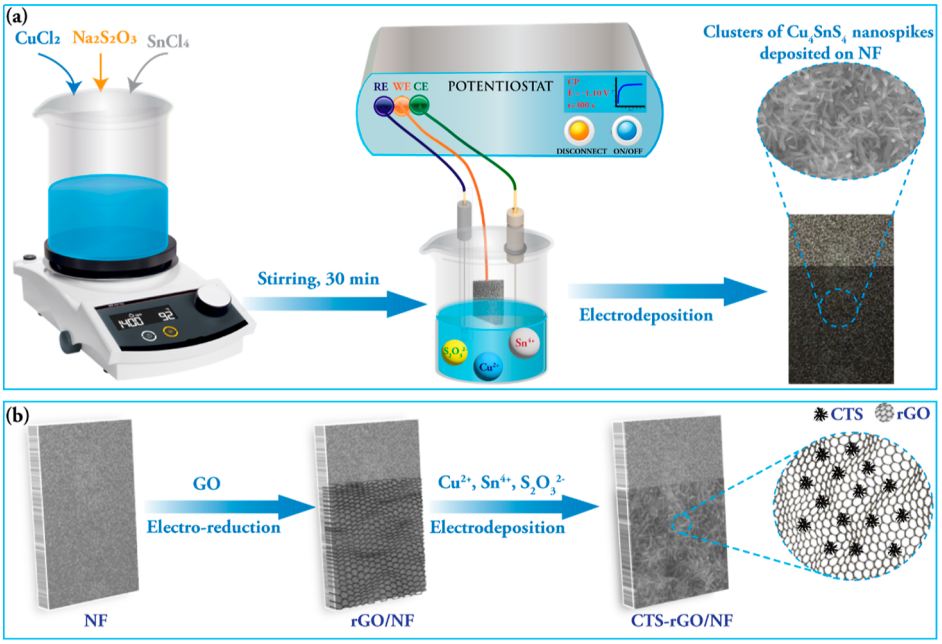

Figure 1. Schematic of the preparation of (a) CTS/NF and (b) CTS−rGO/NF composite electrodes by a facile potentiostatic electrodeposition method.

capacitance but are limited due to poor rate capability and electrical conductivity, while conducting polymer-based electrodes exhibit exceptional electrochemical redox activity but suffer from poor cycle stability.[16] In contrast, transition-metal sulfides offer higher specific capacity, rate capability, and have gained immense attention for the last two decades, owing to their unique morphology and crystal structure, environmental stability, easy availability of precursors, facile synthesis methodologies, and low solubility in most electrolytes.[3,17,18] Among these transition-metal sulfides, more focus has recently been paid to ternary transition-metal sulfides, such as $NiCo_2S_4$,[19,20] $CuCo_2S_4$,[21] $MnCo_2S_4$,[22] and copper tin sulfides (CTS),[23−25] due to their improved performance owing to the existence of multiple metals with differing oxidation states and higher electrical conductivity than binary metal sulfides.[1,22]

CTS (Cu_2SnS_3 and Cu_4SnS_4) compounds have lately fascinated researchers owing to their low cost, low toxicity, excellent electrical conductivity (with hole density reaching up to $\sim 10^{22}$ cm^{-3}), narrow band gap, and reliable chemical and electrochemical stability.[24,26,27] Accordingly, CTS (Cu_2SnS_3 and Cu_4SnS_4) materials have recently been investigated as an electrode material for SCs and batteries with promising results, with Cu_4SnS_4 exhibiting superior performance.[23−25] This could be attributed to enhanced electrical conductivity due to the higher Cu content and defects introduced thereof. Besides, the gap between the voltametric oxidation and reduction peak potentials of Cu_4SnS_4 is smaller than those of other CTS compounds, resulting in improved reversibility of the redox reaction.[26] Furthermore, the existence of a large interplanar spacing in their crystal structure provides enormous and efficient access for ion intercalation, which can undeniably enhance their capacitive performance.[28] Density functional theory calculations have also shown that Cu_4SnS_4 undergoes smaller volumetric expansion and forms more stable electrodes upon ion intercalation−deintercalation for Li battery application.[29]

Despite its potential suitability for SC[24] and battery application,[26,29] there are few studies reporting the application of Cu_4SnS_4 composites as an electrode material for SCs. Compared to other ternary transition-metal sulfides such as $Ni_2Co_2S_4$, the reported performance of the Cu_4SnS_4 electrode is insufficient regarding cycle stability, rate capability, and specific capacity probably resulting from poor electrical conductivity, restacking, and agglomeration of the active material during continued charge−discharge processes.[24]

Hence, a strategy to improve the performance of the Cu_4SnS_4 material must be sought. Such strategies include using a binder-free film deposition technique such as electrochemical deposition and forming a composite with carbon-based materials, notably graphene. Besides its simplicity, the electrochemical deposition method allows for binder-free, direct binding of the electroactive material on the conductive substrate enhancing the effective contact area between active materials and electrolytes, and the substrate thereby effectively reducing the impedance of the electrode for ion and electron transport (charge transfer) leading to the much improved electrochemical performance.[30−33] The performance of the pristine Cu_4SnS_4 materials can also be enhanced by the formation of a composite with graphene. Studies have shown that incorporating reduced graphene oxide (rGO) with transition-metal sulfides has been shown to enhance their capacitive performance by a factor of more than $\sim 1.5\times$ (see Table S1).[10,34,35] Forming a composite with rGO enhances the performance of the active material as it introduces improvements in surface area, electrical conductivity, and structural stability.[36] To the best of our knowledge, electrochemical deposition of copper tin sulfide (Cu_4SnS_4) or Cu_4SnS_4/rGO nanocomposite on the nickel foam (NF) substrate (labeled as CTS/NF and CTS-rGO/NF) for use as SC electrode materials has not been reported yet.

Owing to the excellent intrinsic characteristics of Cu_4SnS_4, simplicity of the electrochemical synthesis method, and advantage offered by the incorporation of rGO along with

https://doi.org/10.1021/acsomega.3c09008
ACS Omega 2024, 9, 9452−9462

the limited research reports available, an attempt has been made to fabricate a high-performance CTS/NF and CTS−rGO/NF nanocomposite electrodes through a facile potentiostatic electrodeposition of Cu_4SnS_4 and rGO on an NF substrate, for use in SCs. The fabricated electrodes were evaluated for SC applications and found to exhibit excellent pseudocapacitive characteristics. Compared with CTS/NF, the CTS/rGO/NF nanocomposite electrode exhibited a high specific capacitance of 820.83 F g^{-1} at a current density of 5 mA/cm^2 [1.6 times that of pristine CTS/NF electrode (516.67 F g^{-1})] ; high-rate capability of 73.1% when the current density increased from 5 to 12 mA/cm^2; and improved cycling stability with a capacitance retention of 92.7% after 1000 continuous galvanostatic charge−discharge (GCD) cycles demonstrating its capability as a promising electrode material for SC application.

2. EXPERIMENTAL SECTION

2.1. Chemicals. Copper(II) chloride dihydrate ($CuCl_2 \cdot 2H_2O$), Tin(IV) chloride tetrahydrate ($SnCl_4 \cdot 4H_2O$), sodium thiosulfate pentahydrate ($Na_2S_2O_3 \cdot 5H_2O$), trisodium citrate, sodium tartarate, NF substrate (1 × 1.5 × 1.7 mm), fluorine-doped tin oxide (FTO)-coated conductive glass substrate, graphite powder (99%, 45 mm), sulfuric acid [H_2SO_4, 98%(m/m)], phosphoric acid (H_3PO_4) potassium permanganate ($KMnO_4$), sodium sulfite (Na_2SO_3), hydrogen peroxide [H_2O_2, 30%(v/v)], hydrochloric acid (HCl), potassium hydroxide (KOH), ethanol, and deionized (DI) water were used for synthesis and characterization of CTS/NF and CTS−rGO/NF composite electrodes.

2.2. Preparation of CTS/NF Electrodes. The (CTS) Cu_4SnS_4 was deposited electrochemically on the NF substrate from a 100 mL solution of an aqueous electrolyte containing 0.04 mol $CuCl_2$, 0.01 mol $SnCl_4$, 0.05 mol $Na_2S_2O_3$, 0.1 mol tartaric acid, and 0.2 mol trisodium citrate at a pH of 5.0 and a cathodic deposition potential of −1.10 V versus Ag/AgCl reference electrode using a three-electrode electrochemical system (IVIUMSTAT potentiostat) for 5 min (Figure 1a) following the procedures described in the literature.[37,38] The as-prepared CTS/NF electrode was then rinsed with distilled water and dried in a vacuum oven at 60 °C for 12 h. The CTS/NF was used as the working electrode with Pt foil and Ag/AgCl serving as the counter and reference electrode, respectively. Before the electrodeposition process, the NF substrate was ultrasonically cleaned with HCl, ethanol, and deionized water consecutively, for 20 min each, respectively.

2.3. Synthesis of Graphene Oxide. Graphene oxide (GO) was synthesized by adopting Marcano's method with slight modifications.[39] Prior to the synthesis, graphite powder and $KMnO_4$ in the ratio of 1:6 were powdered with a mortar and pestle and were precooled to 5 °C in a refrigerator along with a separate mixture of 100 mL of conc. H_2SO_4 and H_3PO_4 mixed in the ratio of 9:1(v/v). The precooled mixtures were then transferred to a larger 1 L beaker and then placed in a chilled water bath and continuously stirred for about 1 h while keeping the temperature below 25 °C; at this stage, the color of the mixture changed to greenish black. The mixture was then heated and continuously stirred for about 12 h in a water bath with the temperature maintained below 55 °C, after which the solution becomes brownish. The mixture was then allowed to cool to room temperature, after which the reaction mixture was poured into a beaker containing 400 mL of ice and cold DI water to quench the reaction followed by the addition of 5 mL of 30%(v/v) H_2O_2 while stirring with a glass rod; after which the color of the solution changed to golden yellow, marking the formation of GO. Additional DI water (400 mL) was then added to the solution after 5 min, then the GO was allowed to settle for an hour, and the supernatant discarded. This was followed by successive washing with 1 M HCl, DI water, ethanol, and deionized water many times with intermediate centrifugation (at 6000 rpm for 10 min) and decantation to obtain a brownish-colored GO gel. Finally, the GO gel was dried at 60 °C under vacuum for about 24 h. The schematic depicting the synthesis of GO is presented in Figure S1.

2.4. Preparation of the CTS−rGO/NF Composite Electrode. The CTS−rGO/NF composite was fabricated by stepwise electrochemical deposition of rGO followed by CTS under slightly different potentials. First the rGO was deposited on an NF substrate by electrochemical reduction of GO ultrasonically dispersed in an electrolyte solution containing Na_2SO_3 using a deposition potential of −1.2 V versus the Ag/AgCl reference electrode. CTS was further electrodeposited on the surface of the rGO/NF substrate at a constant potential of −1.10 V for 5 min from 100 mL of a mixed aqueous solution containing 0.04 mol of $CuCl_2$, 0.01 mol of $SnCl_4$, 0.05 mol of $Na_2S_2O_3$, 0.1 mol of tartaric acid, and 0.2 mol of trisodium citrate at a pH of 5.0 using a three-electrode electrochemical system. The rGO/NF acted as the working electrode with Pt foil and Ag/AgCl electrode acting as counter and reference electrodes, respectively. The fabricated electrode was then rinsed with deionized water and dried at 60 °C in a vacuum oven for 12 h. For XRD characterization, the CTS and CTS-rGO were also deposited on an FTO substrate in a similar way described for their deposition on the NF substrate.

2.5. Material Characterization. The as-prepared materials were extensively characterized by using different techniques. The phase and crystal structure were obtained from the X-ray diffraction patterns obtained by Shimadzu Maxima 7000 X-ray diffractometer and an FEI Tecnai G^2 F20 Super twin transmission electron microscope (TEM) with a beam energy of 300 kV. The morphology and microstructures of CTS/NF and CTS/rGO/NF electrodes were examined using a Hitachi S-4800 scanning electron microscope (SEM) equipped with energy-dispersive spectroscopy (EDS). An UV−visible spectrometer (Azzota. SM-1600) and a Fourier transform infrared spectrometer (PerkinElmer) were also used for characterization of GO.

2.6. Electrochemical Characterization. The electrochemical performances of the electrodes were evaluated through cyclic voltammetry (CV), electrochemical impedance spectroscopy (EIS), and galvanostatic charge−discharge (GCD) techniques using an IVIUMSTAT potentiostat (Ivium Technologies) with the fabricated electrodes functioning as the working electrode, an Ag/AgCl as a reference electrode, and platinum wire as the counter electrode in 1.0 M KOH electrolyte. The constant potential EIS measurements were carried out in the frequency range of 10,000 Hz−0.1 Hz with an AC amplitude of 5 mV and a constant potential of 0.0 V. The CV characterization was carried out within the potential window ranging from 0.0−0.6 V vs Ag/AgCl with a scan rate ranging from 10 to 50 mV/s. The GCD measurements were carried out at different charging/discharging current densities of 5, 6, 7, 8, 10, and 12 mA/cm^2 under an applied potential ranging from 0−0.6 V. To evaluate the cycling capability of CTS/NF and CTS/rGO/NF

https://doi.org/10.1021/acsomega.3c09008
ACS Omega 2024, 9, 9452−9462

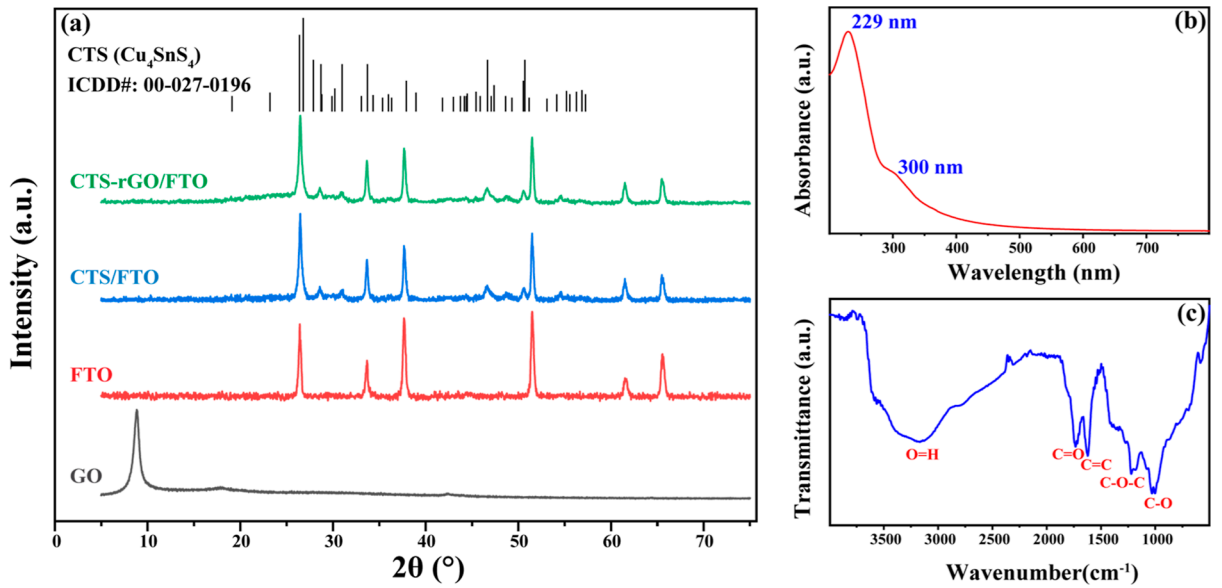

Figure 2. (a) Powder XRD patterns of GO, FTO, CTS/FTO, and CTS−rGO/FTO with reference patterns for orthorhombic Cu_4SnS_4, (b) UV−visible, and (c) FT-IR spectra of GO.

electrodes, GCD cycles were performed at a constant current density of 7 mA/cm^2 within a potential window of 0−0.6 V in 1 M KOH aqueous electrolyte for consecutive 1000 cycles. The specific capacitance (C_S), in F g^{-1}, of the electrode materials was calculated from GCD data using eq 1[35,40]

$$C_{S(GCD)} = \frac{I \times \Delta t}{m \times \Delta V} \quad (1)$$

where Δt is the discharge time in *s*, *I* is the current density per unit area in *mA/cm*^{2}, ΔV is an operating potential window in volts, and *m* is the mass in grams of the deposited electrode material.[24]

3. RESULTS AND DISCUSSION

3.1. Synthesis, Structure, and Morphology Characterization. rGO was deposited on the NF substrate through constant potential cathodic electrochemical reduction of the aqueous GO suspension. During the electrochemical reduction process, the negatively charged GO migrated to the cathode surface and was reduced to rGO. For deposition of CTS on the NF and rGO/NF substrate, a constant cathodic potential of −1.0 V was maintained, prompting the oxidation of thiosulfate ions into sulfide and sulfite ion followed by reduction of Cu^{2+} to Cu^+ by the sulfite ion. The Cu^+ and Sn^{4+} then reacted with the sulfide ion to produce black CTS depositing of the NF substrate. The proposed equations for electrodeposition of CTS are given in eqn. 2−4.[37]

$$4S_2O_3^{2-} + 8e^- \rightarrow 4S^{2-} + 4SO_3^{2-} \quad (2)$$

$$2Cu^{2+} + 4SO_3^{2-} \rightarrow 2Cu^+ + 3SO_4^{2-} \quad (3)$$

$$4Cu^+ + Sn_4^+ + 4S^{2-} \rightarrow Cu_4SnS_4 \quad (4)$$

The schematic of the fabrication of CTS/NF and CTS−rGO/NF electrodes through cathodic electrodeposition of CTS and CTS−rGO on NF substrates is displayed in Figure 1. The optical photographs of the electrode materials (CTS/NF, rGO/NF, and CTS−rGO/NF) are displayed in Figure S2.

Figure 2a displays the XRD patterns of GO powder; bare FTO, CTS/FTO, and CTS−rGO/FTO electrodes. The XRD patterns of the bare FTO substrate, CTS/FTO, and CTS−rGO/FTO displayed six distinct major peaks centered at 2θ values of 26.45, 33.66, 37.64, 51.45, 61.52, and 65.46°, which correspond to the SnO_2 in the FTO substrate (ICDD # 00−046−1088). Besides the characteristic XRD patterns of the FTO substrate, the XRD patterns of CTS/FTO and CTS−rGO/FTO present minor peaks positioned at 2θ values of 26.28, 28.56, 30.93, 46.60, and 50.57°, which can be indexed to the (400), (102), (112), (431), and (223) planes of orthorhombic Cu4SnS4 (ICDD #: 00−027−0196).[41] Furthermore, some XRD peaks of the CTS material may get overlapped with those of the FTO substrate. For GO, the XRD pattern shows a prominent peak at around 2θ = 8.92°, corresponding to a layer-to-layer distance (*d*-spacing) of 0.991 nm, which indicates a very high degree of intercalation, and agrees with values reported in the literature.[39,42] The patterns showed a larger interlayer spacing for GO than graphite powder layers (0.335 nm) due to the insertion of oxygen-containing functional groups between the layers. The absence of graphite's characteristic peak positioned at 2θ = 26° confirmed the sufficient and uniform oxidation level of GO.[43]

Besides XRD, the successful synthesis of GO was confirmed by UV−visible and FT-IR studies. The UV−visible absorption spectra (Figure 2b) recorded for the aqueous suspension of GO showed an absorption peak at 229 nm and the shoulder peak at 300 nm. The peak at 229 nm corresponds to $\pi - \pi^*$ transitions for the C = C bonding, while the broad shoulder at 300 nm corresponds to the $n - \pi^*$ transition of the carbonyl groups (C ═ O) confirming the formation of GO.[35,44] The FT-IR spectra of GO depicted in Figure 2c display peaks revealing the existence of various oxygen containing functional groups such as carbonyl, epoxide, and OH, revealing the successful oxidation of graphite. The broad peak extending from 3100−3400 cm^{-1} is due to the stretching vibration of the − H group. The peaks centered at 1735, 1620, 1224, 1170, and 1030 cm^{-1} correlate to the C ═ O stretching vibration of the carbonyl group, the C ═ C vibration of the skeletal alkene

https://doi.org/10.1021/acsomega.3c09008
ACS Omega 2024, 9, 9452−9462

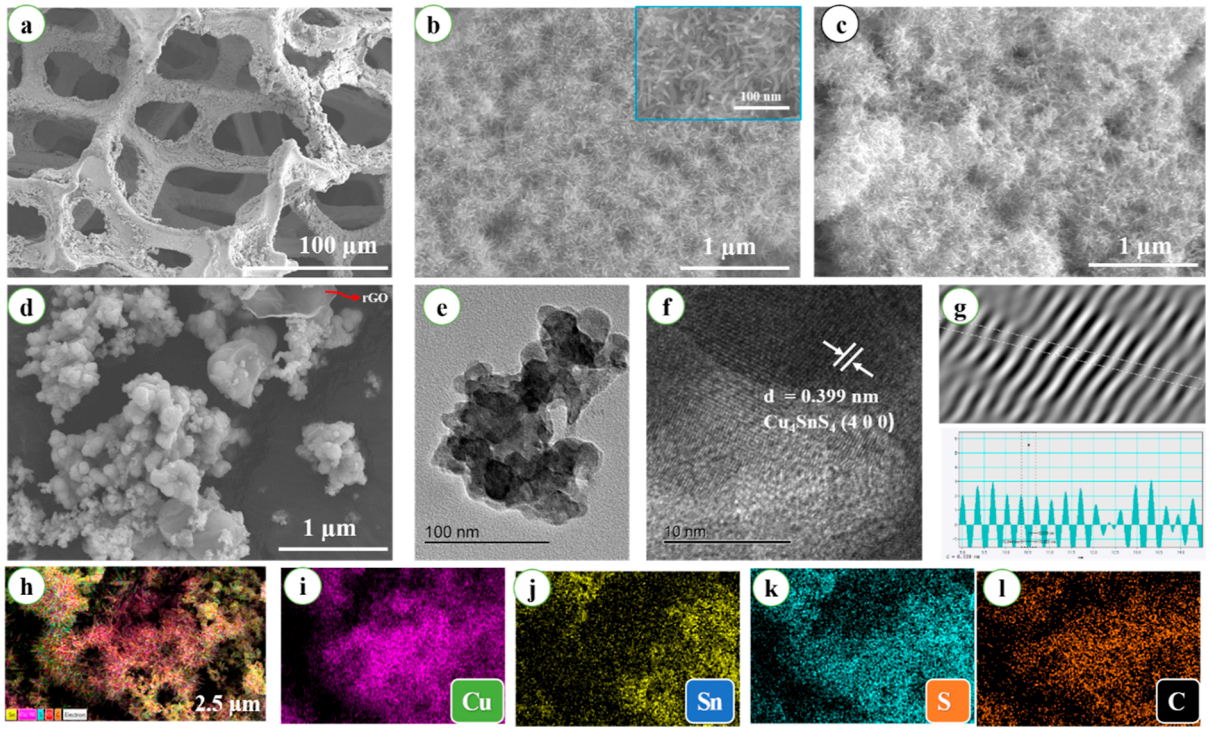

Figure 3. SEM images of (a,b) CTS/NF, (c) CTS-rGO/NF, (d) CTS-rGO; TEM (e), HRTEM (f), IFFT (g), energy-filtered SEM image, and the corresponding EDS elemental mapping for the CTS-rGO composite (h–l).

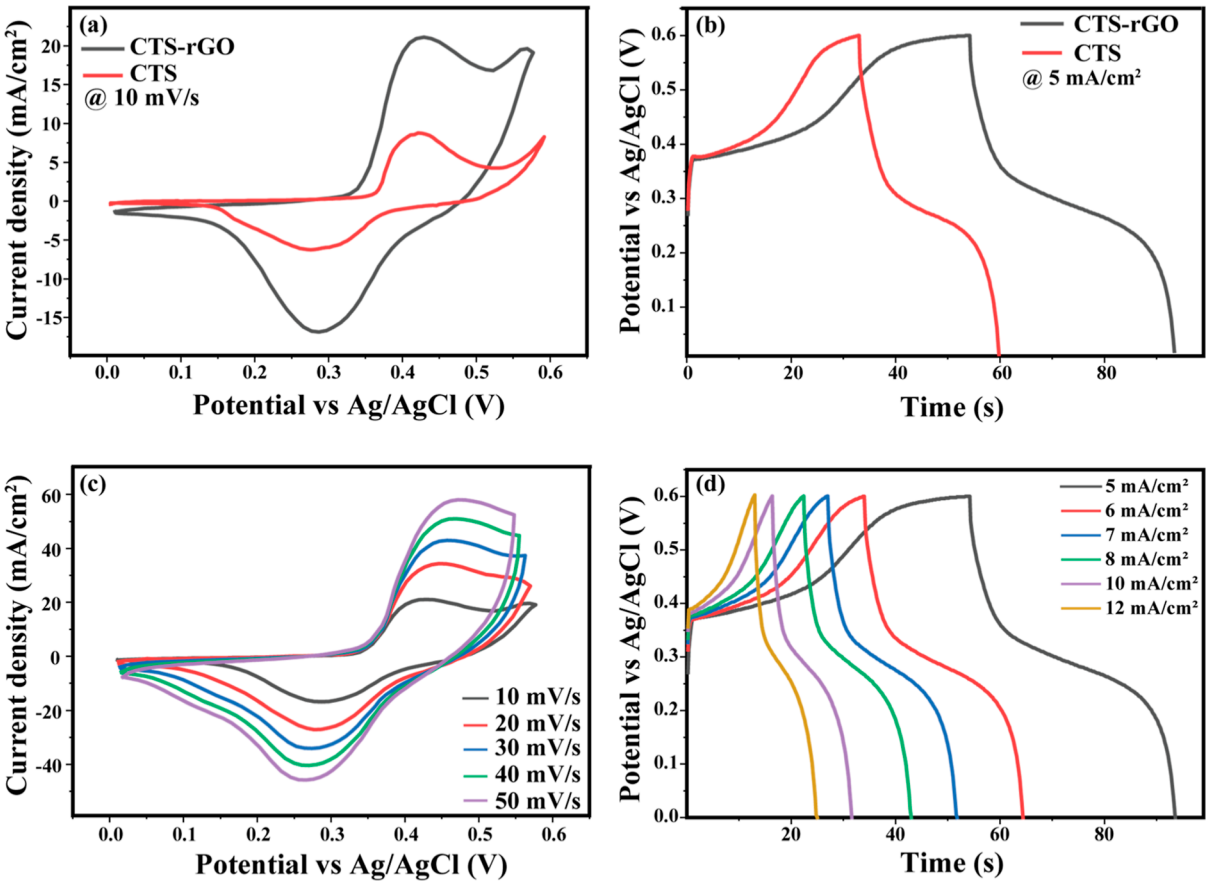

Figure 4. Comparison of (a) CV curves, (b) GCD curves of CTS–rGO/NF and CTS/NF electrodes, (c) CV curves, and (d) GCD curves for rGO–CTS/NF composite electrode tested in 1 M KOH electrolyte.

https://doi.org/10.1021/acsomega.3c09008
ACS Omega 2024, 9, 9452–9462

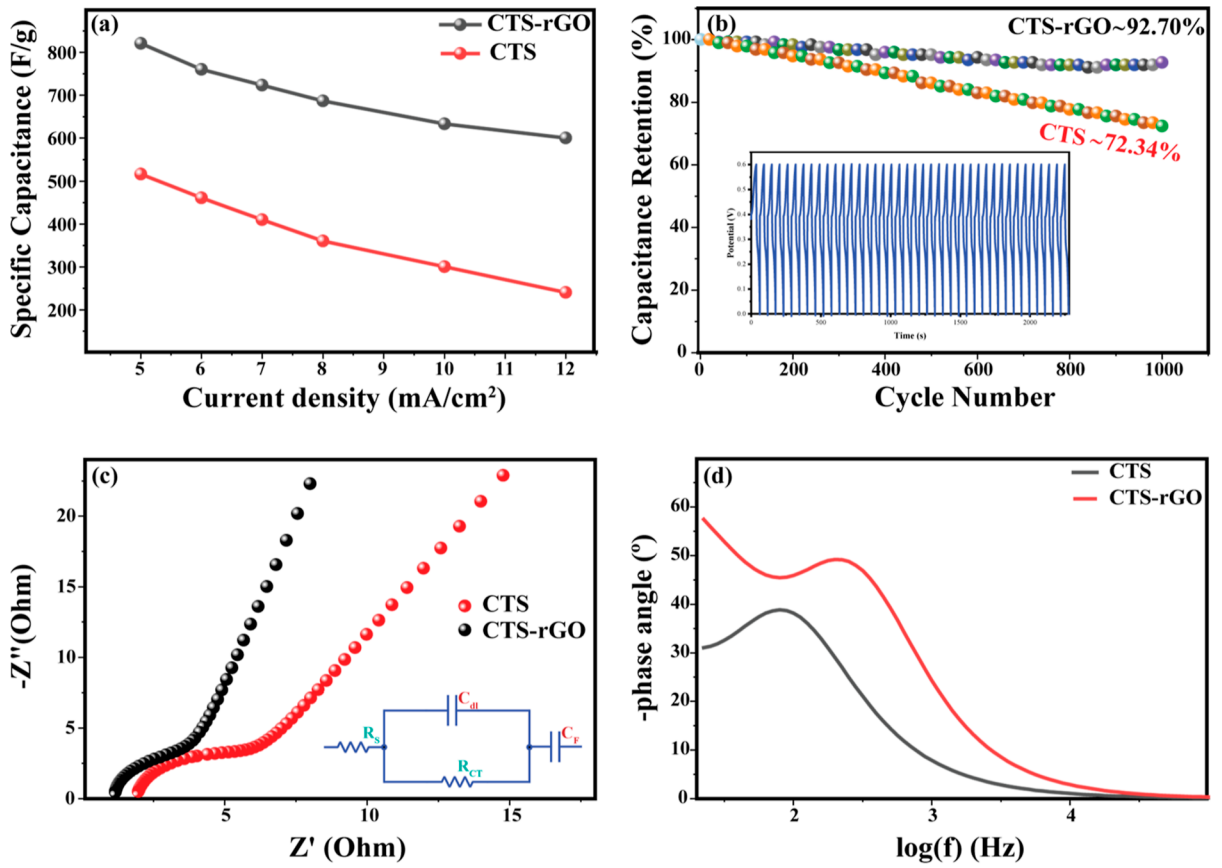

Figure 5. (a) Comparison of C_s of CTS/NF and CTS−rGO/NF at various current densities, (b) capacity retention plots of CTS/NF and CTS−rGO/NF electrodes for 1000 GCD cycle stability test at a current density of 7 mA/cm^2, (c) EIS Nyquist plots of CTS/NF and CTS−rGO/NF, and (d) EIS Bode plot showing phase angle for the CTS/NF and CTS−rGO/NF electrodes.

group, C−OH functional group, and C−O stretching of the epoxide and alkoxy groups, respectively. The presence of alkene, carbonyl, epoxide, alkoxy, and hydroxyl functional group ensures the successful synthesis of GO.[43]

Figure 3a−c displays the SEM images of the CTS/NF and CTS-rGO/NF electrodes at different resolutions. The SEM images reveal interconnected nanospike clusters covering the surface of the NF substrate; the clusters are composed of nanospikes of CTS grown on the NF substrate. Such clusters of nanospikes are capable of providing a high contact area with the electrolyte and a decrease in the diffusion path for ion transfer, thus leading to the enhanced performance. Figure 3d−e depicts the SEM and TEM images, respectively, of the CTS-rGO composite obtained by ultrasonic removal from the NF substrate, revealing the existence of rGO nanosheets in the composite. As shown in Figure 3h−l, the SEM−EDS elemental mapping of the fabricated materials revealed the existence and uniform distribution of the elements Cu, Sn, S, and C. The HRTEM image with the corresponding IFFT obtained by Gatan software (Figure 3f−g) revealed lattice fringes with a lattice spacing of 0.339 nm corresponding to the (4 0 0) planes of orthorhombic phase of Cu_4SnS_4, which is in good agreement with the result of the XRD analysis.

3.2. Electrochemical Performance Evaluation. The electrochemical performance of CTS/NF and CTS−rGO/NF composite electrodes was evaluated by various techniques including CV, GCD, and EIS. A typical three-electrode cell configuration with Ag/AgCl and Pt wire serving as the reference and counter electrodes, respectively, and the CTS/NF or CTS−rGO/NF as the working electrode with 1 M KOH solution as an electrolyte were used for the electrochemical evaluation of the fabricated electrode materials.

For CV characterization of the electrode materials, a potential range of 0.0−0.6 V was maintained over various voltage scan rates ranging from 10−50 mV/s in 1 M aqueous KOH electrolyte. CV analysis was used to identify the existence and contribution of faradic and nonfaradic processes for the charge storage mechanism. Figure 4a presents comparison of CV curves of CTS/NF and CTS−rGO/NF at a scan rate of 10 mV/s within a potential range of 0.0−0.6 V. The CV curves exhibit a pair of redox peaks that agree with the typical behavior of CTS (Cu_2SnS_3 and Cu_4SnS_4) materials reported previously,[23−25] indicating pseudocapacitive, battery type, and faradic behavior. The pair of redox peaks for CTS/NF and CTS−rGO/NF occur at about 0.45 and 0.26 V; 0.43 and 0.25 V, respectively. The anodic peak can be attributed to the reaction: $Cu^+ \rightarrow Cu^{2+}$ or $Sn^{2+} \rightarrow Sn^{4+}$; while that of the cathodic peak corresponds to the reaction: $Cu^{2+} \rightarrow Cu^+$ or $Sn^{4+} \rightarrow Sn^{2+}$.[24] Moreover, from the CV plot, it can be noted that the CTS−rGO/NF electrode showed a higher peak current density, larger area under the curve, and reduced peak separation potential than the pristine CTS/NF electrode, revealing the enhanced capacitive performance of the CTS−rGO/NF electrode material. The increased capacitance for CTS−rGO/NF can be attributed to the synergistic involvement of the conductive and high surface graphene layers, which also protected the CTS nanospike clusters from collapse and agglomeration.[35]

https://doi.org/10.1021/acsomega.3c09008
ACS Omega 2024, 9, 9452−9462

CV curves of the CTS/NF and CTS−rGO/NF electrodes at different scan rates are displayed in Figures S3a and 4c, respectively. A pair of distinct redox peaks can be observed for both electrodes at various scan rates. As the scan rate increased from 10 to 50 mV/s, the anodic peaks shifted to a higher potential while cathodic peaks shifted to a lower potential, which may be due to resistive effects involved with the electrode, polarization, and fast electrode kinetics with the increasing scan rate, consistent with the quasi-reversible characteristics of the redox reaction.[45,46] Besides, the peak current increased proportionally with the increase in the scan rate with no sign of peak attenuation, indicating good reversibility of the quasi-redox reactions and hence excellent pseudocapacitive behavior. From CV plots, the capacity of the SC electrode is directly proportional to the absolute area of the CV curve and inversely proportional to the value of the scan rate, suggesting that higher capacity is achieved at low scan rates. The higher capacitance at the lower scan rate could be credited to the efficient diffusion reaction of the electrolyte with the internal electroactive sites of the electrode. At higher scan rates, the electrolyte ions cannot efficiently interact with the electrode material, so the electrode material cannot be utilized sufficiently resulting in lower capacitance.[47] Moreover, the peak currents correlate linearly with the inverse of the square root of the scan rate, suggesting domination of the diffusion controlled faradic redox processes for charge storage.[22,40]

Along with CV, the performance of the electrode materials was also evaluated by its charging−discharging capabilities at varied current densities. As shown in Figure 4b, the GCD curves of both CTS/NF and CTS−rGO/NF electrodes exhibit nonlinear curves, different from the triangular GCD curves of Electrochemical double-layer capacitor (EDLCs) indicating battery-type pseudocapacitive behavior. The GCD curves are almost symmetrical, indicating a rapid current−voltage response and excellent electrochemical reversibility of the electrode material. Voltage plateaus are in the range of 0.4−0.5 and 0.2−0.3 V for the charge and discharge curves, respectively, consistent with the redox peaks observed in the CV curves. It can be noted that the CTS−rGO/NF electrode exhibited enhanced capacitive performance than the CTS/NF electrode, as evidenced by the longer discharge times.

Figures 4d and S3b depict GCD curves of the CTS−rGO/NF and CTS/NF electrode materials, respectively, at various charge−discharge current densities ranging from 5 to 12 mA/cm^2. The specific capacitance, Cs (F g^{-1}), of the electrode materials was calculated using eq 1 and yielded a value of 820.83, 760.00, 723.33, 686.67, 633.33, and 600.00 F g^{-1} at current densities of 5, 6, 7, 8, 10, and 12 mA/cm^2, respectively, for the CTS−rGO/NF electrode material, while that of bare CTS/NF electrode recorded a much lower capacitance value of 516.67, 460.83, 410.01, 360.21, 300.02, and 240.11 F g^{-1}. It can be observed that at all current densities, the specific capacitance of the CTS−rGO/NF electrode is higher than that of the CTS/NF electrode. Figure 5a depicts the variation in specific capacitance of the CTS/NF and CTS−rGO/NF electrodes, as calculated from GCD data. As observed from the results, the CTS−rGO/NF electrode retained 73.1% of its initial capacitance at a current density of 12 mA/cm^2, with the CTS/NF electrode retaining only 46.5% of its initial capacitance, suggesting the enhanced performance of the composite electrode as evidenced by its higher capacitance values and rate capability. The enhanced performance of the CTS−rGO/NF electrode could be attributed to the enhancement in conductivity along with increased surface area due to the introduction of rGO. Moreover, the results show that for both electrode materials, Cs decreased as the current density increases, which is related to the kinetics of the electrode reactions. The higher capacitance at the lower current densities results from the efficient interaction of the electrolyte with the internal electroactive sites of the electrode, while at higher current densities, the electrolyte ions cannot efficiently interact with the electrode material due to the diffusion-limited electrode kinetics, so the active utilization of the electrode material is low resulting in lower capacitance.[45] Additionally, other factors such as higher IR losses and concentration polarization could be responsible for reduced capacitance at higher current densities.[17]

Long-term continuous charge−discharge cycling or the cycling stability of the electrode is a critical issue and an important parameter for practical SC applications. The cycling stability of the electrode materials was evaluated by running a continuous GCD cycle for about 1000 cycles at a constant current density of 7 mA/cm^2. For the CTS/NF electrode, as depicted in the capacitance retention plot (Figure 5b), the capacitance gradually decreases and maintains a capacitance retention of 72.34% of the initial value, while the CTS−rGO/NF electrode capacitance retention of 92.70% of the initial value was maintained after the 1000 GCD cycles, which is much higher than that of the bare CTS/NF electrode. The results demonstrated the good cycling stability of the CTS−rGO/NF composite electrode and its suitability in SC application.

Charge-transfer ability, conductivity, and the associated resistance of the energy storage electrode at the electrode−electrolyte interface were evaluated using EIS. The EIS measurement was further utilized to investigate rGO's role in enhancing the capacitive performance of the CTS−rGO/NF composite electrode. EIS curves of the CTS/NF and CTS−rGO/NF electrodes are shown in Figure 5c. All spectra consisted of a typical semicircle, followed by a straight line. The high-frequency region in the spectra provides information about the electrode and electrolyte resistance (R_S). The diameter of the semicircle in the spectrum relates to the resistance arising from the charge-transfer (R_{CT}) kinetics, which is associated with the electrode/electrolyte interface. The line gradient in the low-frequency region measures the diffusion resistance called the Warburg impedance (W).[35] For the CTS−rGO/NF electrode, a relatively vertical slope was observed in the low-frequency area compared to that of the CTS/NF electrode, which reveals the lower diffusion resistance between the working electrode and the electrolyte. The values, of R_S, R_{CT}, were obtained by fitting the EIS spectra with the equivalent circuit shown in the inset of Figure 5c. Through the EIS fitting, the CTS−rGO/NF electrode yielded a smaller R_S of 1.13 Ω, relative to that of the CTS/NF electrode (1.89 Ω). Moreover, the CTS−rGO/NF electrode exhibited a smaller R_{CT} of 2.23 Ω compared to that of the CTS/NF electrode (3.22 Ω), revealing the improved charge-transfer ability of the CTS−rGO/NF electrode relative to that of the CTS/NF electrode. This demonstrated a fact that the high conductivity and large-surface area of rGO ensured both the lower charge transfer and ion diffusion resistance and enhanced capacitive performance. Moreover, the Bode phase angle plot (Figure 5d) indicates that the phase angle measured in the low-frequency region for CTS−rGO/NF is 76.2°, which

https://doi.org/10.1021/acsomega.3c09008
ACS Omega 2024, 9, 9452−9462

Table 1. Summary of Supercapacitive Performance of CTS-Based Materials Reported in the Literature with Reference to This Work

electrode material	potential window (V)	electrolyte	specific capacitance (F g^{-1})	cycling stability (%/cycle)	reference
Cu_2SnS_3	0.13−0.53	3 M KOH	1015 @1 A g^{-1}	60/2000 @2 A g^{-1}	23
Cu_4SnS_4	0.0−0.50	1 M NaOH	684 @20 mA/cm^2	72/2000 @40 mA/cm^2	24
Cu_2SnS_3	0.1−0.65	1 M KOH	183 @1 A g^{-1}	88.5/2000 @1 A g^{-1}	25
Cu_4SnS_4	0.0−0.60	1 M KOH	516.67 @5 mA/cm^2	72.3/1000 @7 mA/cm^2	**This work**
Cu_4SnS_4−rGO	0.0−0.60	1 M KOH	820.83 F @5 mA/cm^2	92.7% ; 1000 @7 mA/cm^2	

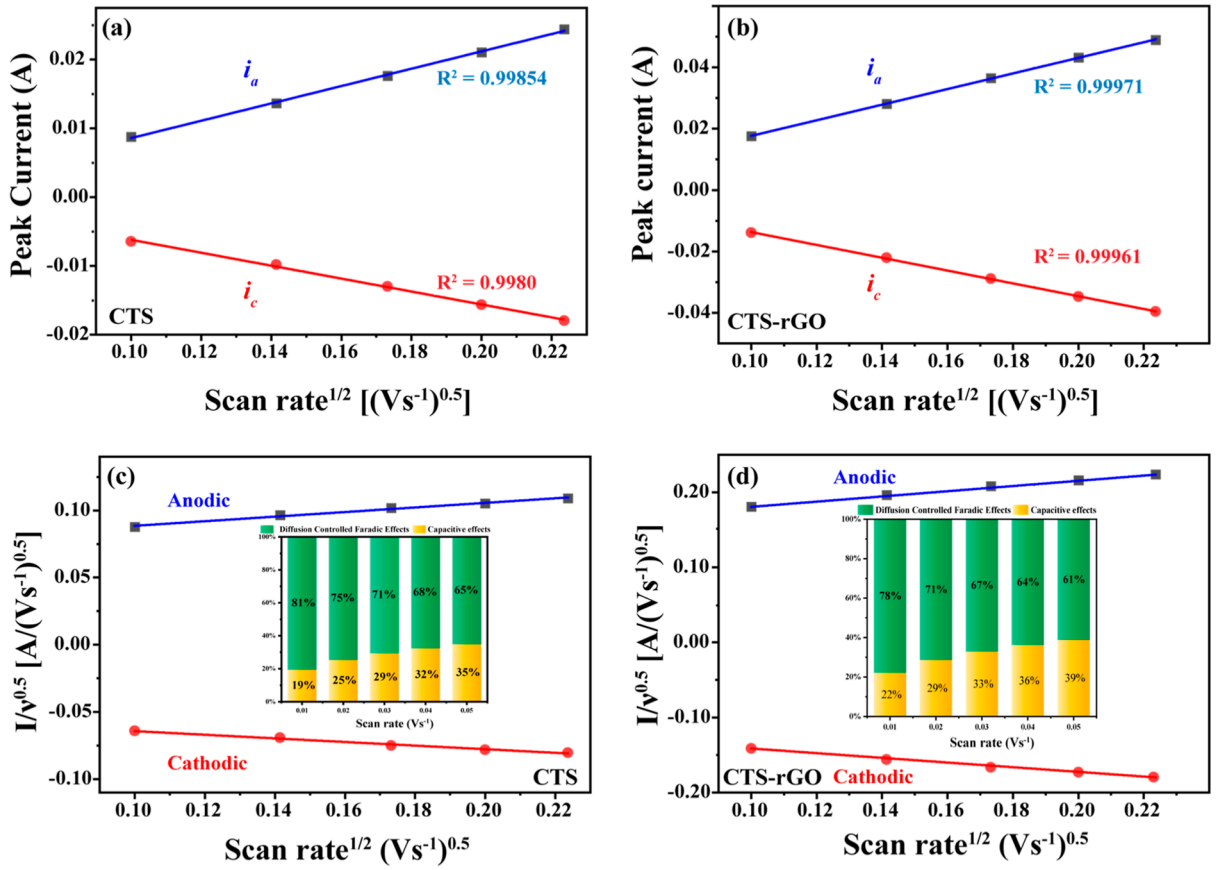

Figure 6. Linear fit plot of (a,b) peak current (I) vs. square root of scan rate ($\upsilon^{1/2}$); (c,d) $I/\upsilon^{1/2}$/ vs. $\upsilon^{1/2}$ with insets of % contribution of diffusion controlled faradic processes and capacitive processes under different scan rates, as derived from CV data of CTS/NF and CTS−rGO/NF electrodes, respectively.

is higher than pristine CTS/NF electrode (55.5°), further demonstrates the enhanced capacitive nature of the CTS−rGO/NF composite electrode.[35]

Overall, electrochemical evaluations of the fabricated materials revealed the enhanced performance of the CTS−rGO/NF electrode. The performance of the fabricated electrode materials reported in this paper is better than CTS-based materials reported in the literature, as shown in Table 1.[23−25]

3.3. Supercapacitor Charge Storage Mechanism. The capacitance of the SC electrode arises from capacitive (cap.), faradic and nonfaradic surface processes, and diffusion (diff.) controlled faradic processes that occur deep inside the electrode, as given in eq 5.[18] The contribution of the capacitive and diffusion-controlled processes at different voltage scan rates can be determined from CV data using an eq 6 that relates current (I) to the voltage scan rate (υ)[7,53]

$$I = I_{cap} + I_{diff} \tag{5}$$

$$I = a\upsilon^b \tag{6}$$

$$\log(I) = \log(a) + b\log(\upsilon) \tag{7}$$

where a and b represent constant and are determined from the intercept and slope, respectively, of the plot of log(I) vs. log(υ), eq 7. The value of b is used for the kinetic study of the electrode processes, and it determines the extent of contribution of the capacitive and diffusion processes for the charge storage mechanism involved in the electrode, where a value of b = 1 indicates presence of capacitive fast faradic and nonfaradic processes occurring at the surface of the electrode, while a value of b = 0.5 indicates a sluggish, diffusion-controlled, battery-type faradic process.[18,50] A b value of 0.643 and 0.654 was obtained for the cathodic peak currents (i_c) of the CTS/NF and CTS−rGO/NF electrodes (Figure S4a,b), revealing the existence of both capacitive and diffusion-controlled processes, with the diffusion-controlled process as a dominant contributor to the charge storage mechanism.

https://doi.org/10.1021/acsomega.3c09008
ACS Omega 2024, 9, 9452−9462

For capacitive processes, the peak current (I) response changes linearly with the scan rate (υ), while that of diffusion-controlled processes peak current response changes linearly with the square root of the scan rate ($\upsilon^{1/2}$) and can be expressed using the eq 8[3,18]

$$I = k \times \upsilon + k_2 \times \upsilon^{0.5} = I_{cap} + I_{diff} \quad (8)$$

$$I \times \upsilon^{-0.5} = k_1 \times \upsilon^{0.5} + k_2 \quad (9)$$

The value of k_1 and k_2 was determined from the slope and intercept, respectively, of the linear fit plot of $I/\upsilon^{1/2}$ vs. $\upsilon^{1/2}$ [eq. 9]. As displayed in Figure 6a,b, the plots of both anodic (i_a) and cathodic peak currents (i_c) vs. $\upsilon^{1/2}$ fit linearly with $R^2 >$ 0.99 for both CTS/NF and CTS−rGO/NF electrodes, further confirming the dominance of diffusion controlled faradaic processes for the charge storage mechanism. Besides, the contribution of the capacitive and diffusion controlled process for the charge storage at different voltage scan rates (10−50 mV/s) for the CTS/NF and CTS−rGO/NF electrodes is shown in the insets of Figure 6c,d, with the capacitive contribution increasing from 19−35 and 22−39%; while the contribution of the diffusion-controlled process decreased from 81−65 and 78−61% as the scan rate increased from 10−50 mV/s, for the CTS/NF and CTS−rGO/NF electrode, respectively.

The observed decrease in the I_{diff} and increase in I_{cap} as the scan rate increased can be understood based on the kinetics of the electrochemical reactions occurring at the electrode−electrolyte interface. At high scan rates, electrolyte ions do not have enough time to diffuse and reach to the electrode surface to undergo sufficient redox reaction; hence, the capacitive process prevails at the electrode surface due to fast charge/discharge faradic and nonfaradic processes occurring at the electrode−electrolyte interface as that of EDLCs. Meanwhile, at lower scan rates, the electrolyte ions enjoy sufficient time to diffuse and reach to the electrode surface to participate in the faradic charge-transfer processes.[18]

4. CONCLUSIONS

In this work, flower-like clusters of nanosheet of CTS were deposited electrochemically on NF and rGO/NF substrates to fabricate CTS/NF and CTS−rGO/NF electrodes for SC application. The CTS−rGO/NF electrode exhibited the highest performance with specific capacitance of 820.83 F g^{-1} compared with the bare CTS/NF electrode (516.67 F g^{-1}) at a current density of 5 mA/cm^2 ; rate capability of 73.1% as compared with 46.5% for CTS/NF for current densities ranging from 5−12 mA/cm^2. Moreover, the CTS−rGO/NF electrode exhibited better capacitance retention of 92.7% as compared to the CTS/NF (72.34%) electrode after continuous 1000 GCD cycles at a current density of 7 mA/cm^2. The enhanced performance of CTS−rGO/NF is attributed to the synergetic effect of the enhanced conductivity and surface area introduced by the integration of rGO. Furthermore, the introduced rGO layer maintains the structural integrity of the electrode by preventing the collapse of the CTS nanosheet clusters. In conclusion, this work demonstrated CTS−rGO/NF nanocomposite as a promising electrode material for high-performance SC application.

ASSOCIATED CONTENT

Supporting Information

The Supporting Information is available free of charge at https://pubs.acs.org/doi/10.1021/acsomega.3c09008.

Comparison of supercapacitive performance of various pristine materials and their composites with rGO or graphene; synthesis of GO; optical photographs of rGO, CTS, and CTS−rGO electro deposited on NF and FTO; CV and GCD profiles of the CTS/NF electrode in 1 M aqueous KOH electrolyte in the potential range of 0.0−0.6 V; and linear fit plot of log(I) vs. log(υ) for CTS/NF and CTS−rGO/NF electrodes, as derived from CV data obtained for scan rates ranging from 10 to 50 mV/s (PDF)

AUTHOR INFORMATION

Corresponding Authors

Endale Kebede Feyie − *Department of Applied Chemistry, Adama Science and Technology University, Adama 1888, Ethiopia;* Present Address: Department of Chemistry, Dire Dawa University, P.O. Box: 1362, Dire Dawa, Ethiopia; orcid.org/0000-0001-7461-0707; Email: endex01@gmail.com

Enyew Amare Zereffa − *Department of Applied Chemistry, Adama Science and Technology University, Adama 1888, Ethiopia*; Email: enyewama@yahoo.com

Authors

Lemma Teshome Tufa − *Department of Applied Chemistry, Adama Science and Technology University, Adama 1888, Ethiopia; Research Institute of Materials Chemistry, Chungnam National University, Daejeon 34134, Republic of Korea;* orcid.org/0000-0001-6929-8464

Jaebeom Lee − *Research Institute of Materials Chemistry, Chungnam National University, Daejeon 34134, Republic of Korea; Department of Chemistry, Department of Chemistry Engineering and Applied Chemistry, Chungnam National University, Daejeon 34134, Republic of Korea;* orcid.org/0000-0002-8414-7290

Aschalew Tadesse − *Department of Applied Chemistry, Adama Science and Technology University, Adama 1888, Ethiopia;* orcid.org/0000-0001-6962-1479

Complete contact information is available at: https://pubs.acs.org/10.1021/acsomega.3c09008

Author Contributions

The manuscript was written through the contributions of all authors. All authors have approved the final version of the manuscript.

Notes

The authors declare no competing financial interest.

ACKNOWLEDGMENTS

The authors would like to thank Postgraduate program of Adama Science and Technology University, Research and Technology Transfer Office, Adama Science and Technology University (ASTU) (no. ASTU/AS-R/013/2021) and Dire-Dawa University, Dire Dawa, Ethiopia, for financially supporting this research. This work was supported by the National Research Foundation of Korea (NRF2019R1A2C2007825 and NRF-2017R1A4A1015627).

https://doi.org/10.1021/acsomega.3c09008
ACS Omega 2024, 9, 9452−9462

REFERENCES

(1) Abdel Maksoud, M. I. A.; Fahim, R. A.; Shalan, A. E.; Abd Elkodous, M.; Olojede, S. O.; Osman, A. I.; Farrell, C.; Al-Muhtaseb, A. H.; Awed, A. S.; Ashour, A. H.; Rooney, D. W. Advanced Materials and Technologies for Supercapacitors Used in Energy Conversion and Storage: A Review. *Environ. Chem. Lett.* **2021**, *19* (1), 375−439.

(2) Majumdar, D. Recent Progress in Copper Sulfide Based Nanomaterials for High Energy Supercapacitor Applications. *J. Electroanal. Chem.* **2021**, *880*, 114825.

(3) Liu, W.; Niu, H.; Yang, J.; Cheng, K.; Ye, K.; Zhu, K.; Wang, G.; Cao, D.; Yan, J. Ternary Transition Metal Sulfides Embedded in Graphene Nanosheets as Both the Anode and Cathode for High-Performance Asymmetric Supercapacitors. *Chem. Mater.* **2018**, *30*, 1055−1068.

(4) Wang, H.; Casalongue, H. S.; Liang, Y.; Dai, H. $Ni(OH)_2$ Nanoplates Grown on Graphene as Advanced Electrochemical Pseudocapacitor Materials. *J. Am. Chem. Soc.* **2010**, *132* (21), 7472−7477.

(5) Lokhande, V. C.; Lokhande, A. C.; Lokhande, C. D.; Kim, J. H.; Ji, T. Supercapacitive Composite Metal Oxide Electrodes Formed with Carbon, Metal Oxides and Conducting Polymers. *J. Alloys Compd.* **2016**, *682*, 381−403.

(6) Pan, Y.; Xu, K.; Wu, C. Recent Progress in Supercapacitors Based on the Advanced Carbon Electrodes. *Nanotechnol. Rev.* **2019**, *8* (1), 299−314.

(7) Yang, M.; Cheng, H.; Gu, Y.; Sun, Z.; Hu, J.; Cao, L.; Lv, F.; Li, M.; Wang, W.; Wang, Z.; Wu, S.; Liu, H.; Lu, Z. Facile Electrodeposition of 3D Concentration-Gradient Ni-Co Hydroxide Nanostructures on Nickel Foam as High Performance Electrodes for Asymmetric Supercapacitors. *Nano Res.* **2015**, *8* (8), 2744−2754.

(8) Patil, S. J.; Dubal, D. P.; Lee, D. Gold Nanoparticles Decorated RGO-$ZnCo_2O_4$ Nanocomposite: A Promising Positive Electrode for High Performance Hybrid Supercapacitors. *Chem. Eng. J.* **2020**, *379*, 122211.

(9) Vidhya, M. S.; Ravi, G.; Yuvakkumar, R.; Velauthapillai, D.; Thambidurai, M.; Dang, C.; Saravanakumar, B. Nickel-Cobalt Hydroxide: A Positive Electrode for Supercapacitor Applications. *RSC Adv.* **2020**, *10* (33), 19410−19418.

(10) Isacfranklin, M.; Ravi, G.; Yuvakkumar, R.; Kumar, P.; Velauthapillai, D.; Saravanakumar, B.; Thambidurai, M.; Dang, C. Urchin like $NiCo_2O_4$/RGO Nanocomposite for High Energy Asymmetric Storage Applications. *Ceram. Int.* **2020**, *46* (10), 16291−16297.

(11) Barqi, J.; Masoudpanah, S. M.; Liu, X.; Sh. Bafghi, M.; Ong, C. K. Fabrication of Porous Cu_2S Nanosheets for High Performance Hybrid Supercapacitor. *J. Energy Storage* **2022**, *45* (July 2021), 103781.

(12) Karade, S. S.; Dwivedi, P.; Majumder, S.; Pandit, B.; Sankapal, B. R. First Report on a FeS-Based 2 V Operating Flexible Solid-State Symmetric Supercapacitor Device. *Sustainable Energy Fuels* **2017**, *1* (6), 1366−1375.

(13) Mishra, R. K.; Baek, G. W.; Kim, K.; Kwon, H.-I.; Jin, S. H. One-Step Solvothermal Synthesis of Carnation Flower-like SnS_2 as Superior Electrodes for Supercapacitor Applications. *Appl. Surf. Sci.* **2017**, *425*, 923−931.

(14) Theerthagiri, J.; Karuppasamy, K.; Durai, G.; Rana, A.; Arunachalam, P.; Sangeetha, K.; Kuppusami, P.; Kim, H.-S. Recent Advances in Metal Chalcogenides (MX; X = S, Se) Nanostructures for Electrochemical Supercapacitor Applications: A Brief Review. *Nanomaterials* **2018**, *8* (4), 256.

(15) Liu, X.; Qi, X.; Zhang, Z.; Ren, L.; Liu, Y.; Meng, L.; Huang, K.; Zhong, J. One-Step Electrochemical Deposition of Nickel Sulfide/Graphene and Its Use for Supercapacitors. *Ceram. Int.* **2014**, *40* (6), 8189−8193.

(16) Wu, W.; Yang, L.; Chen, S.; Shao, Y.; Jing, L.; Zhao, G.; Wei, H. Core-Shell Nanospherical Polypyrrole/Graphene Oxide Composites for High Performance Supercapacitors. *RSC Adv.* **2015**, *5* (111), 91645−91653.

(17) El-Hout, S. I.; Mohamed, S. G.; Gaber, A.; Attia, S. Y.; Shawky, A.; El-Sheikh, S. M. High Electrochemical Performance of RGO Anchored CuS Nanospheres for Supercapacitor Applications. *J. Energy Storage* **2021**, *34* (July), 102001.

(18) Setayeshmehr, M.; Haghighi, M.; Mirabbaszadeh, K. Binder-Free 3D Flower-like Alkali Doped- SnS_2 Electrodes for High-Performance Supercapacitors. *Electrochim. Acta* **2021**, *376*, 137987.

(19) Xin, C.; Ang, L.; Musharavati, F.; Jaber, F.; Hui, L.; Zalnezhad, E.; Bae, S.; Hui, K. S.; Hui, K. N. Supercapacitor Performance of Nickel-Cobalt Sulfide Nanotubes Decorated Using Ni Co-Layered Double Hydroxide Nanosheets Grown in Situ on Ni Foam. *Nanomaterials* **2020**, *10* (3), 584.

(20) Liu, C.; Wu, X. $NiCo_2S_4$ Nanotube Arrays Grown on Flexible Carbon Fibers as Battery-Type Electrodes for Asymmetric Supercapacitors. *Mater. Res. Bull.* **2018**, *103*, 55−62.

(21) Fan, L.; Pan, F.; Tu, Q.; Gu, Y.; Huang, J.-L.; Huang, Y.-F.; Wu, J.-H. Synthesis of $CuCo_2S_4$ Nanosheet Arrays on Ni Foam as Binder-Free Electrode for Asymmetric Supercapacitor. *Int. J. Hydrogen Energy* **2018**, *43* (52), 23372−23381.

(22) Han, X.; Xuan, H.; Gao, J.; Liang, T.; Yang, J.; Xu, Y.; Han, P.; Du, Y. Construction of Manganese-Cobalt-Sulfide Anchored onto RGO/Ni Foam with a High Capacity for Hybrid Supercapacitors. *Electrochim. Acta* **2018**, *288*, 31−41.

(23) Wang, C.; Tian, H.; Jiang, J.; Zhou, T.; Zeng, Q.; He, X.; Huang, P.; Yao, Y. Facile Synthesis of Different Morphologies of Cu_2SnS_3 for High-Performance Supercapacitors. *ACS Appl. Mater. Interfaces* **2017**, *9* (31), 26038−26044.

(24) Lokhande, A. C.; Patil, A.; Shelke, A.; Babar, P. T.; Gang, M. G.; Lokhande, V. C.; Dhawale, D. S.; Lokhande, C. D.; Kim, J. H. Binder-Free Novel Cu_4SnS_4 Electrode for High-Performance Supercapacitors. *Electrochim. Acta* **2018**, *284*, 80−88.

(25) Hussain, S. K.; Yu, J. S. Surfactant-Free One-Pot Hydrothermal Growth of Micro-Flower-Like Copper Tin Sulfide Electrode Material for Pseudocapacitor Applications. *J. Electrochem. Soc.* **2018**, *165* (11), E592−E597.

(26) Lin, J.; Lim, J.; Youn, D. H.; Liu, Y.; Cai, Y.; Kawashima, K.; Kim, J.; Peng, D.; Guo, H.; Henkelman, G.; Heller, A.; Mullins, C. B. Cu_4SnS_4 -Rich Nanomaterials for Thin-Film Lithium Batteries with Enhanced Conversion Reaction. *ACS Nano* **2019**, *13* (9), 10671−10681.

(27) Olatunde, O. C.; Onwudiwe, D. C. Selective Syntheses of Kuramite (Cu_2SnS_3) and Petrukite (Cu_3SnS_4) Phases of Copper Tin Sulphide, and Their Electrochemical and Photocatalytic Properties. *Results Mater.* **2022**, *13*, 100249.

(28) Wu, C.; Hu, Z.; Wang, C.; Sheng, H.; Yang, J.; Xie, Y. Hexagonal Cu_2SnS_3 with Metallic Character: Another Category of Conducting Sulfides. *Appl. Phys. Lett.* **2007**, *91* (14), 143104.

(29) Lin, J.; Lim, J.; Youn, D. H.; Kawashima, K.; Kim, J.; Liu, Y.; Guo, H.; Henkelman, G.; Heller, A.; Mullins, C. B. Self-Assembled Cu - Sn - S Nanotubes with High (De)Lithiation Performance. *ACS Nano* **2017**, *11*, 10347−10356.

(30) Biswal, A.; Panda, P. K.; Acharya, A. N.; Mohapatra, S.; Swain, N.; Tripathy, B. C.; Jiang, Z.; Minakshi Sundaram, M. Role of Additives in Electrochemical Deposition of Ternary Metal Oxide Microspheres for Supercapacitor Applications. *ACS Omega* **2020**, *5* (7), 3405−3417.

(31) Jin, K.; Zhou, M.; Zhao, H.; Zhai, S.; Ge, F.; Zhao, Y.; Cai, Z. Electrodeposited CuS Nanosheets on Carbonized Cotton Fabric as Flexible Supercapacitor Electrode for High Energy Storage. *Electrochim. Acta* **2019**, *295*, 668−676.

(32) Chai, Z.; Wang, Z.; Wang, J.; Li, X.; Guo, H. Potentiostatic Deposition of Nickel Cobalt Sulfide Nanosheet Arrays as Binder-Free Electrode for High-Performance Pseudocapacitor. *Ceram. Int.* **2018**, *44* (13), 15778−15784.

(33) Kadam, S. L.; Bulakhe, R. N.; Kadam, R. A.; Yewale, M. A. Electrochemical Synthesis of CuS Thin Film for Supercapacitor Application. *Macromol. Symp.* **2020**, *392* (1), 1900209.

(34) Ravuri, S.; Pandey, C. A.; Ramchandran, R.; Jeon, S. K.; Grace, A. N. Wet Chemical Synthesis of SnS/Graphene Nanocomposites for

https://doi.org/10.1021/acsomega.3c09008
ACS Omega 2024, 9, 9452−9462

High Performance Supercapacitor Electrodes. *Int. J. Nanosci.* **2018**, *17* (01n02), 1760022.
(35) Lonkar, S. P.; Pillai, V. V.; Patole, S. P.; Alhassan, S. M. Scalable In Situ Synthesis of 2D-2D-Type Graphene-Wrapped SnS_2 Nanohybrids for Enhanced Supercapacitor and Electrocatalytic Applications. *ACS Appl. Energy Mater.* **2020**, *3* (5), 4995−5005.
(36) Geng, P.; Zheng, S.; Tang, H.; Zhu, R.; Zhang, L.; Cao, S.; Xue, H.; Pang, H. Transition Metal Sulfides Based on Graphene for Electrochemical Energy Storage. *Adv. Energy Mater.* **2018**, *8* (15), 1703259.
(37) Guo, Y.; Yin, X.; Yang, Y.; Que, W. Construction of ZnO/Cu_2SnS_3 Nanorod Array Films for Enhanced Photoelectrochemical and Photocatalytic Activity. *RSC Adv.* **2016**, *6* (106), 104041−104048.
(38) Khattak, Y. H.; Baig, F.; Toura, H.; Harabi, I.; Beg, S.; Soucase, B. M. Single Step Electrochemical Deposition for the Fabrication of CZTS Kesterite Thin Films for Solar Cells. *Appl. Surf. Sci.* **2019**, *497* (May), 143794.
(39) Marcano, D. C.; Kosynkin, D. V.; Berlin, J. M.; Sinitskii, A.; Sun, Z.; Slesarev, A.; Alemany, L. B.; Lu, W.; Tour, J. M. Improved Synthesis of Graphene Oxide. *ACS Nano* **2010**, *4* (8), 4806−4814.
(40) Sajjad, M.; Khan, Y.; Lu, W. One-Pot Synthesis of 2D SnS_2 Nanorods with High Energy Density and Long Term Stability for High-Performance Hybrid Supercapacitor. *J. Energy Storage* **2021**, *35* (January), 102336.
(41) Zhang, X.; Tang, Y.; Wang, Y.; Shen, L.; Gupta, A.; Bao, N. Simple One-Pot Synthesis of Cu_4SnS_4 Nanoplates and Temperature-Induced Phase Transformation Mechanism. *CrystEngComm* **2020**, *22* (7), 1220−1229.
(42) Ranjan, P.; Agrawal, S.; Sinha, A.; Rao, T. R.; Balakrishnan, J.; Thakur, A. D. A Low-Cost Non-Explosive Synthesis of Graphene Oxide for Scalable Applications. *Sci. Rep.* **2018**, *8* (1), 12007.
(43) Trikkaliotis, D. G.; Mitropoulos, A. C.; Kyzas, G. Z. Low-Cost Route for Top-down Synthesis of over- and Low-Oxidized Graphene Oxide. *Colloids Surf., A* **2020**, *600* (March), 124928.
(44) Yu, H.; Zhang, B.; Bulin, C.; Li, R.; Xing, R. High-Efficient Synthesis of Graphene Oxide Based on Improved Hummers Method. *Sci. Rep.* **2016**, *6* (1), 36143.
(45) Isacfranklin, M.; Yuvakkumar, R.; Ravi, G.; Hong, S. I.; Shini, F.; Thambidurai, M.; Dang, C.; Velauthapillai, D. Marigold Flower like Structured Cu_2NiSnS_4 Electrode for High Energy Asymmetric Solid State Supercapacitors. *Sci. Rep.* **2020**, *10* (1), 19198.
(46) Jiang, J.; Chen, Y.; Hu, X.; Cong, H.; Zhou, Q.; Rong, H.; Sun, Y.; Han, S. Designed Synthesis of 2D Multilayer $CuCo_2S_4$ Nanomaterials for High-Performance Asymmetric Supercapacitors. *Vacuum* **2020**, *182* (June), 109698.
(47) Li, X.; Zhou, K.; Zhou, J.; Shen, J.; Ye, M. CuS Nanoplatelets Arrays Grown on Graphene Nanosheets as Advanced Electrode Materials for Supercapacitor Applications. *J. Mater. Sci. Technol.* **2018**, *34* (12), 2342−2349.

https://doi.org/10.1021/acsomega.3c09008
ACS Omega 2024, 9, 9452−9462